Geometry-based Stochastic Channel Model for High Speed Railway Communications

Lai Zhou, Fengyu Luan, Shidong Zhou, *Member, IEEE*, Andreas F. Molisch, *Fellow, IEEE*, and Fredrik Tufvesson, *Fellow, IEEE*

***Abstract*—Reliable wireless communications links are a critical but challenging aspect for high speed railway (HSR). To develop and analyze such systems, accurate models for the propagation channel are required. The radio channel properties in HSR scenarios are different from those in cellular scenarios not only due to the high velocity, but also due to the special construction elements and the type of surroundings along the train lines. We performed a measurement campaign at a carrier frequency of 2.4 GHz on the Guangzhou-Shenzhen dedicated high-speed train line in China. Motivated by the results from these measurements, we propose the concept of *active scatterer region* as an improvement for geometry-based stochastic channel models for HSR, to better describe the non-stationary properties of such channels. Further contributions to the total channel impulse response are also studied, including the line-of-sight component and the scattering component from overhead line poles. Each type of component is modeled and fully parameterized based on the measurement results.**

***Index Terms*—High speed railway, GSCM, channel measurement, non-stationary, active scatterer region.**

I. Introduction

High speed railways (HSRs) are well established as an important form of mass transportation. They are widely deployed, especially in the areas of high population density, due to their capability of moving large number of people at high speed, and with high energy efficiency. As examples, the operation of the Japanese Shinkansen started in 1964, and is commonly regarded as the first HSR in the world. European systems, such as France's TGV starting in 1981, Italy's Direttissima starting in 1988, German's ICE starting in 1991, Spain's AVE starting in 1992, together build an efficient HSR network [1]. China is extending its infrastructure and is currently the country with the most extensive network of HSR [2].

HSR requires good communication capabilities for two main applications: (i) providing train passengers with internet access for voice and data; (ii) sending/receiving control information and safety-relevant data between the trains and the HSR infrastructure [3]. The existing Global System for Mobile Communication Railway (GSM-R) can only provide a data rate up to 200 kb/s [4]. Future systems are anticipated to use more advanced modulation/multiple access systems such as orthogonal time frequency space (OTFS) modulation [5] and/or multi radio access technology (RAT) [6]. Development and analysis of such systems require special channel models that reflect the following features of HSR: (i) non-wide-sense-stationarity; (ii) rapid time variability and large Doppler shift caused by the high speed. These features were verified in our previous HSR papers [7]-[10] and could be inferred from investigations in other vehicular communications channel models [11][12].

There are a number of papers investigating the HSR channel characteristics in different scenarios, including viaducts [13]-[15], tunnels [16][17] and cuttings [18]-[20]. However, most of HSR channel modeling papers concentrate on path loss and fading characteristics, and they typically use purely stochastic models where the channel variation is modeled as a stationary random process. Although such models are simple and convenient for generating channel samples for system simulation and analysis, the models are only suitable for a drop based simulation, and can not represent the non-stationary channel process due to the movement of the train. Geometry-based stochastic channel models (GSCMs) provide a way to overcome this problem, since they have been found to be well suited for modeling non-wide-sense stationary uncorrelated scattering (non-WSSUS) channels [21][22]. In existing GSCMs, for the simulation of each sample process, a set of scatterers with randomly assigned characteristics (locations and scattering factors, etc.) are generated and fixed during this sample process, thus the channel (including strength, delay, direction of arrival (DOA), direction of departure (DOD)) could be changing with the movement of the train. Compared with purely stochastic models, GSCMs provide better physical correspondence, and often match better with measurement

Manuscript received June 30, 2018; revised December 13, 2018; accepted February 25, 2019. The work of Lai Zhou and Shidong Zhou was funded by the projects as follows, National S&T Major Project (2017ZX03001011), National Natural Science Foundation of China (61631013), Foundation for Innovative Research Groups of the National Natural Science Foundation of China (61621091), Tsinghua-Qualcomm Joint Project, Future Mobile Communication Network Infrastructure Virtualization and Cloud Platform (2016ZH02-3). The work of Fengyu Luan was funded partly by a Tsinghua-USC student exchange scholarship. The work of Andreas F. Molisch was partly funded by the National Science Foundation (NSF) under projects ECCS-1731694 and ECCS-1126732. The review of this paper was coordinated by Prof. T. Kuerner. (*Corresponding author: Shidong Zhou.*)

Lai Zhou is with the Key Laboratory of Particle and Radiation Imaging, Department of Engineering Physics, Tsinghua University, Beijing, China (e-mail: zhoulai09@gmail.com).

Fengyu Luan is with the State Grid Ziguang Microelectronics Technology Limited Company, Beijing, China (e-mail: luanfy1987@gmail.com).

Shidong Zhou is with the Department of Electronic Engineering, Tsinghua University, Beijing, China (e-mail: zhousd@tsinghua.edu.cn).

A. F. Molisch is with the Ming Hsieh Department of Electrical and Computer Engineering, Viterbi School of Engineering, University of Southern California, Los Angeles, CA 90089, USA (e-mail: molisch@usc.edu).

F. Tufvesson is with the Department of Electrical and Information Technology, Lund University, SE22100 Lund, Sweden (e-mail: fredrik.tufvesson@eit.lth.se).

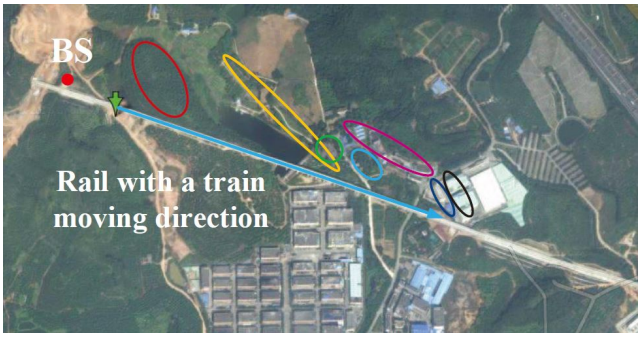

Fig. 1: Satellite image of the measured scenario.

results [23]-[25].

There have been some GSCMs for HSR proposed in the literature: [26] proposes a three-dimension (3D) GSCM in a mountainous scenario, but all scatterers contribute with the same power and the positions of scatterers are fixed. [27]-[29] focus on cutting scenarios, but the scatterers are distributed uniformly on the slope of the cutting or a virtual cylinder, and the scattering components are always seen while the train is moving. [30]-[32] express the change of the position of effective scatterers in an ellipse or a circle around the receiver based on theoretical analysis. However, the distribution of scatterers should depend on the realistic environments. For example, the surrounding scatterers are usually mountains, forests and buildings along the railway, covering a large area.

From measurement data we have recorded from a train traveling on a viaduct in a hilly environment, we identified some important characteristics. With the movement of the train or the observation point, the positions of some scatterers seem to be changing. Actually, we think this phenomenon can be explained by either a birth-and-death of different scattering points, or the reflection phenomena, resulting in a change of the reflecting point on a surface. Although some existing models also include the birth-and-death effect, they do not model such events of different scatterers relatively, and thus cannot express the phenomenon of smoothly changing sets of scatterers that was observed in the measurement. Motivated by the visibility region concept in the COST 259 and COST 2100 channel model for cellular communications [33][34], we define an *active scatterer region* to express the movement of scatterers with the motion of the train. However, the COST 2100 model does not deal with the temporal variations of the visibility region, which turned out to be essential to properly model the observed behavior. In addition, based on the measurements, many other important aspects of the channel are also found, including a certain lifetime of the active scatterer region, the geometrical relationship between the location of physical scatterers and the movement speed of scatterers, etc..

The main contributions of this paper are summarized as follows.

- Based on the idea of active scatterer regions varying with the train movement, we propose an accurate and practical GSCM for HSR.
- We provide model parameters for a GSCM based on a measurement campaign in a hilly terrain scenario. The special HSR infrastructure is also parameterized in this model, such as overhead line poles close to the tracks.

The remainder of the paper is organized as follows: In Section II, a brief description of the measurement campaigns is presented. Based on the detection and analysis of the scattering points from the measured data, in Section III we propose a model where the active scatterer region varies with the motion of the train. Section IV gives an implementation recipe for a practical HSR GSCM, including the typical modeling parameters. Section V verifies the improved GSCM through a comparison with the original measurements. Section VI concludes the paper and outlines possible future developments.

II. Measurement Campaign

A HSR measurement campaign was conducted on the Guangzhou-Shenzhen dedicated high-speed line to provide channel data for modeling. Parameters of the multipath components (MPCs) are extracted as reference data for our proposed GSCM in this paper. More details about the measurement campaign can be found in [7][8].

A. Measurement setup

A wideband channel sounder similar to that in [35] with center frequency of 2.4 GHz is used for the measurements. The descriptions of the transmitter (TX), the receiver (RX) and the test signal are outlined below.

- Transmitter: An S-Wave-25-65-18DV10 panel antenna produced by Netop is used as the TX antenna [7], due to the possibility for installation at the GSM base station (BS) tower. The BS tower is located 10 m to the left of the rails with respect to the train direction of motion, and the bottom of the TX antenna is 30 m above the railway. The antenna is directional and the main beam is oriented parallel along the tracks in azimuth with 65° horizontal and 7° vertical beam-widths, which results in 17 dBi gain at the 2.4 GHz carrier frequency. When the train is far from the BS, the gain of the TX antenna is approximately constant, though it drops when the train is near the BS. The sounding signal is fed through a power amplifier to the TX antenna with a total conducted power of 20 dBm, and the Effective Isotropic Radiated Power (EIRP) is 37 dBm.
- Receiver: The RX antenna is a vertically polarized and horizontally omnidirectional antenna with 7 dBi gain. It is fixed on one of the left windows inside the carriage with respect to the train movement direction, with an average penetration loss of approximately 26 dB. The antenna height is 1.2 m above the rail. The received intermediate frequency signal is sampled at a rate of 100 Msamples/s and stored to a hard disk array for further off-line analysis. The TX and RX are locked to two Rubidium clocks that have been well synchronized before the measurement to reduce frequency offset as much as possible.
- Test signal: The test signal is a linear frequency modulated (LFM) signal with a bandwidth of 40 MHz and a length of 12.8 μs. The peak to off-peak ratio of the

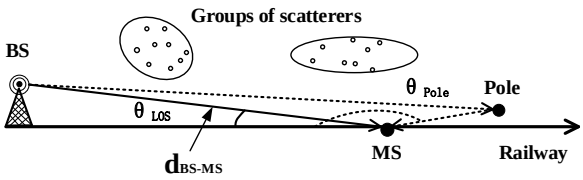

Fig. 2: Geometrical description of the channel environment.

autocorrelation function is 22 dB, so that the channel impulse responses can be obtained by calculating the correlation between the received signals and the original signal.

The channel impulse response is sampled every 25.6 μs, which includes a waiting time of 12.8 μs before the transmission of next test signal, i.e., the maximum observable delay of a MPC is 3840 m. In general, the velocity of the train is almost constant within a local region. Therefore, a uniform sampling in time is equal to a uniform sampling in space.

B. Measured HSR scenario

The measured scenario is a suburban area with low rounded hills. Fig. 1 shows the satellite image of the measured area. The GPS coordinates of the BS are (22.830558N, 113.860235E). The measured route is the white line with a blue arrow, which indicates the movement direction of the train. The red dot represents the position of the BS. The total length of the measured route is about 1000 m. The TX antenna mounted on the BS tower is elevated and close to the rail, so the line-of-sight (LOS) path typically dominates the channel impulse response. Different groups of scatterers are also illustrated in this map using ellipses, such as small hills, forests, roads, buildings and houses. Note that the virtual uniform linear array (ULA) is constructed with an element spacing of $\lambda/2$ and 16 branches to obtain spatial characterization, and we cannot distinguish between MPCs incident from the left or right. However, due to the MS antenna pattern and its placement on a left window, MPCs from the left are emphasized (Appendix B), and we assume in the following that all MPCs are coming from that left side.

The velocity monitoring system of the train reported a velocity of 295 km/h (Appendix A). There is no other train going in the same or different directions during the measurement. The special construction elements used for HSRs give rise to some specific properties of the propagation environment that are quite common in most HSR lines in China. For example, the overhead line poles are spaced 50 m apart to provide the electricity. The distance between each pole to the track is less than 1.5 m. As will be discussed later, we find that the overhead line pole will act as both major static scatterers and as obstructions to the LOS path.

III. Active Scatterer Region Results and Modeling

A. HSR channel characteristics

Fig. 2 depicts the environment geometrically where the trace of the moving receiver is used as an axis, with positive direction as the moving direction. The mobile station (MS)

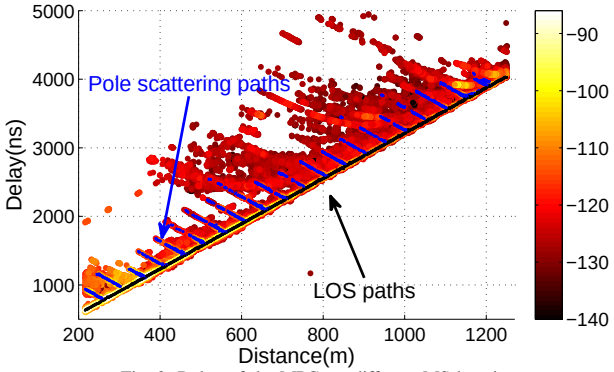

Fig. 3: Delay of the MPCs at different MS locations.

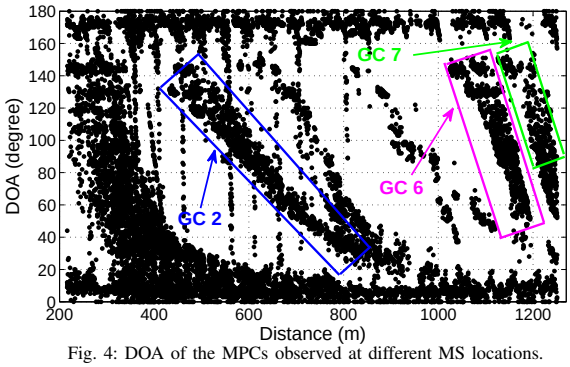

Fig. 4: DOA of the MPCs observed at different MS locations.

at each location on the axis could receive the LOS path and many other MPCs coming from surrounding scatterers, including the poles. d_{BS-MS} is the distance between BS and MS, θ_{LOS} and θ_{Pole} are the DOAs of LOS path and pole scattering path, respectively. The Subspace Alternating Generalized Expectation-maximization (SAGE) algorithm [36] is used to obtain estimates of the MPCs from the measurements, i.e., amplitude, delay and DOA.

Fig. 3 shows the power-delay-profile observed at different distances of the MS from the BS. The extracted LOS paths are plotted as the black lines, and the periodically emerging paths plotted with blue lines are inferred to be the pole scattering (PS) paths. Apart from the LOS and PS paths, there are some time-continuous varying MPCs, which come from scatterers with geometrically similar locations, e.g., buildings and hills. Fig. 4 depicts the DOA of MPCs observed at different MS locations. Since the BS is very close to the rail, when the distance d_{BS-MS} is larger than 100 m, the DOA of the LOS path can be regarded as almost 0. However, the DOA of the path from other scatterers may change with the movement of the MS. Taking the scattered path from a pole as an example, when the MS is moving towards the pole, the DOA of this path changes from near 180 degree to 90 degree, while when the MS passes by the pole and then moves far past it, its DOA changes from 90 degree to approximately 0.

From Fig. 3 and Fig. 4, we may conclude the following:

- The set of delays and DOAs at different MS locations are different, i.e., the channel is non-stationary;
- The change of delays and DOAs of the MPCs at adjacent MS locations are similar, i.e., the parameters of the MPCs at different MS locations are correlated, implying that a model with multiple groups of paths might be suitable;

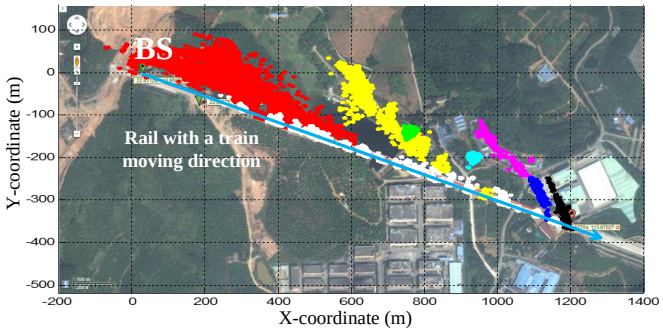

Fig. 5: scatterers emerged during the whole measurement.

TABLE I: Scatterers detected in HSR scenario

No.	Color	Scattering objects
1	Red	Forest
2	Yellow	Trees around hill
3	Green	Houses
4	Blue green	Trees
5	Purple	Buildings
6	Blue	Buildings
7	Black	Buildings
8 – 27	White	Poles

- Based on the single-scattering assumption, locations of the scatterers of all these paths can be found [9]. By plotting the scatterer location data for MPCs at different MS locations, we also see the effect of continuously changing scatterer locations;
- The scatterers of different paths are associated with different locations, and may have different changing properties (affecting the change of delay and DOA);
- Some paths may have close scatterer locations and similar changing properties, i.e., these geometrically concentrated paths behave in a similar way with respect to MS motion for quite a long distance.

As mentioned in [9], some of the scatterers are classified into several geometrical clusters (GCs) by using a K-power-means based clustering algorithm. The GC is a group of geometrically concentrated scatterers on a map, so that their associated MPCs have similar long-term properties [9]. Figure 5 shows the detection result of GCs with different colors. The light blue line with arrow shows the railway and the direction of the train's movement. By comparing the locations of the scatterers of each GC with the satellite image, we find the physical source of the scatterers as listed in Table I, while the white objects are detected poles along the railway.

In order to model the dependence of GC on the motion of MS, we define the active scatterer region (ASR) as a region of scatterers of the GC, giving rise to MPCs that have significant amplitude *at a given time* (i.e., for a given location of the MS). As the train moves along the railway, the ASR varies its position, giving rise to changes of the active scatterers, i.e., a birth/death process of the scatterers and associated MPCs. The corresponding delays and azimuths of scattering paths change smoothly in a similar way during a significant time period (corresponding to significantly long moving distance of the MS). For example, the rectangles with different colors in Fig. 4 show the changing DOAs resulting from active scatterers in the ASRs of different GCs. Besides, the ASR has a finite lifetime, i.e., when the ASR does not overlap the area in which there are scatterers of the GC, the ASR is "dead".

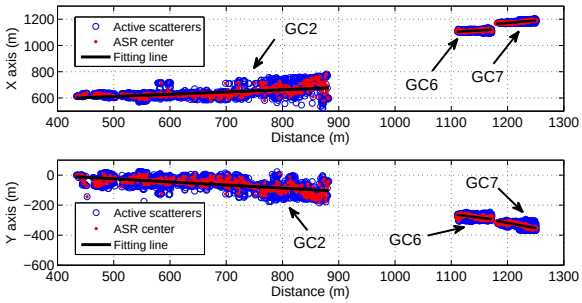

Fig. 6: The "moving" center of the active scatterer region.

B. The principle of the ASR model

The parameters of the scatterers are evaluated at different sample locations (spaced approximately 0.5 m apart), at which the set of scatterers may be different. The power weighted center $\vec{\boldsymbol{C}}_{S,r}(t)$ at different times (locations) can be calculated to express the motion of the center of the ASR,

$$\vec{\boldsymbol{C}}_{S,r}(t) = \frac{\sum_{l=1}^{L_{S,r}(t)} G_{S,r,l}(t)\vec{\boldsymbol{Z}}_{S,r,l}(t)}{\sum_{l=1}^{L_{S,r}(t)} G_{S,r,l}(t)}, \tag{1}$$

where $G_{S,r,l}(t)$ is the gain of the l^{th} active scatterer in the ASR of r^{th} GC at time t, and $\vec{\boldsymbol{Z}}_{S,r,l}(t) = (x_{S,r,l}(t), y_{S,r,l}(t))$ is the location of such scatterer. $L_{S,r}(t)$ is the number of the active scatterers in the ASR of r^{th} GC. Fig. 6 shows the "moving" ASR centers of three GCs in X/Y axis and their fitting lines, and the corresponding active scatterers are marked by blue circles. It is clear from the figure that:

- Each ASR has a finite lifetime, e.g., ASR in GC2 exists when the distance between BS and MS is from 433 m to 882 m, or a lifetime of 5.52 s at 295 km/h train speed;
- The center of the ASR moves with the movement of the receiver;
- The movement of the center of the ASR can be approximately modeled as linear with distance, though we observe some statistical fluctuations around that model;
- The active scatterers have spatial spread in each observation location.

The ASRs are typically assigned to GCs in such a way that when the scatterers of the GC are inside the region, the MPCs resulting from such scatterers are active (contribute to the impulse response). For simplicity, we use a circular region to express the shape of ASR as below,

$$\boldsymbol{B}_{S,r}(t) = \{\vec{\boldsymbol{Z}}_{S,r,l}(t), \|\vec{\boldsymbol{P}}_{S,r,l}(t)\| \leq R_{S,r}\}, \tag{2}$$

where

$$\vec{\boldsymbol{P}}_{S,r,l}(t) = \vec{\boldsymbol{Z}}_{S,r,l}(t) - \vec{\boldsymbol{C}}_{S,r}(t) = (\Delta x_{S,r,l}(t), \Delta y_{S,r,l}(t)), \tag{3}$$

$\boldsymbol{B}_{S,r}(t)$ is the set of active scatterers in an ASR of r^{th} GC at time t, $\vec{\boldsymbol{P}}_{S,r,l}(t)$ is the deviation of l^{th} scatterer from the

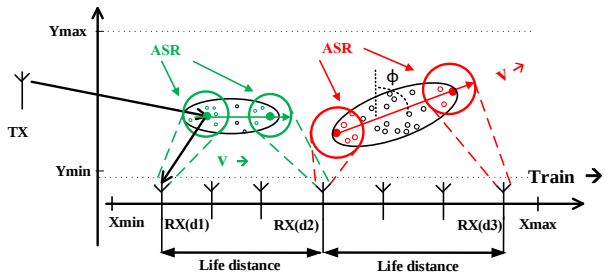

Fig. 7: The principle of the ASR model.

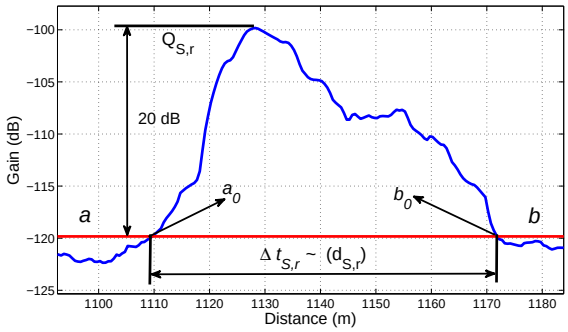

Fig. 8: The definition of lifetime in the GC 6.

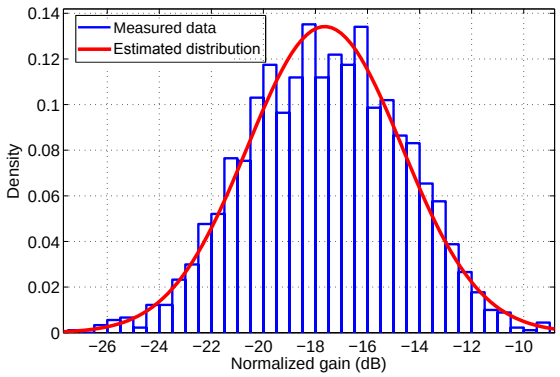

Fig. 9: The distribution of the normalized gains of MPCs in the GC 2.

center of ASR, and $\|\cdot\|$ denotes the magnitude of a vector. $R_{S,r}$ is the corresponding radius of ASR of r^{th} GC. It is important to note that some scatterers (especially for scatterers with weak strengthes) may be out of the region, because the circular region is a regular one and the radius is assumed to be constant for simplicity, which is a trade-off between accuracy and tractability in the modeling.

For system analysis of a non-stationary channel, a model that can characterize the changing properties of a relatively long channel process is needed. Hence, we use a moving ASR to model the birth-and-death process of scatterers, which may include the following important items:

- The motion of the center, which results in non-stationary properties;
- Spatial spread of the scatterers, which leads to delay spread and angular spread, resulting in frequency selectivity and spatial selectivity;
- The lifetime of the ASR, which determines the time during which the scatterers in the ASR impact the channel response. Actually, this quantity is implied in the dimension of the GC, the size of the ASR, and the movement speed of the ASR center.

Considering all the above elements, the general principle is described in Fig. 7: at each observation time (location) along the rail, only a subset of the scatterers is active, i.e., the ASR consists of the scatterers in a circle. The ASR changes its location in a certain direction ϕ and a certain speed v as the train moves, so the RX could "see" the changing scatterers in different observation locations (e.g., RX(d1) $\rightarrow$ RX(d2)). The ASR is modeled as a circular region with a given fixed diameter, and the scatterers are distributed randomly with a certain density in the GC. If the RX and its corresponding ASR does not overlap with the GC anymore, it will mean the end of the lifetime of the GC. The life distance $d_{S,r}$ is defined as the moving distance of RX during the lifetime, and r denotes the index of the GC.

C. Parameterization of the ASR model

- **The motion of the center**

Based on the measurement data shown in Fig. 6, the location vector of the active center of ASR in the r^{th} GC at time t can be modeled as a line with a constant regression coefficient vector,

$$\vec{\boldsymbol{C}}_{S,r}(t) = \vec{\boldsymbol{C}}_{S,r,0} + \vec{\boldsymbol{v}}_{S,r} \cdot (t - t_{S,r,0}), \tag{4}$$

where $\vec{\boldsymbol{C}}_{S,r,0} = [C_{S,r,x,0}, C_{S,r,y,0}]$ is the initial location of the center based on the fitting result, and $\vec{\boldsymbol{v}}_{S,r}$ is the "moving" speed. t is the observation time, $t \in [t_{S,r,0}, t_{S,r,0} + \Delta t_{S,r}]$, $t_{S,r,0}$ is the start time and $\Delta t_{S,r}$ is the active time period, i.e., the lifetime. Note that the "moving" speed is a vector with a direction of $\phi_{S,r}$. The relative speed is expressed as $v_{S,r,0} = \| \vec{\boldsymbol{v}}_{S,r} \| / \| \vec{\boldsymbol{v}}_{train} \|$, and $\vec{\boldsymbol{v}}_{train}$ is the speed of train. Hence, the life distance is expressed as $d_{S,r} = \| \vec{\boldsymbol{v}}_{train} \| \Delta t_{S,r}$.

- **The lifetime of the ASR**

As shown in Fig. 8, the lifetime corresponding to the life distance is defined as

$$\max_{t \in (-\infty, a) \bigcup (b, +\infty)} [G_{S,r}(t)] < Q_{S,r} - 20, \tag{5}$$

$$\Delta t_{S,r} = \min_{a,b} |b - a|, \tag{6}$$

where $G_{S,r}(t)$ is the total gain of the active scatterers in the ASR of r^{th} GC, i.e., $G_{S,r}(t) = \sum_{l=1}^{L_{S,r}(t)} G_{S,r,l}(t)$, and $Q_{S,r}$ is the peak of gain in dB. a and b are the variables used to calculate the lifetime in (6), while the corresponding ranges determined by (5) are $a \leqslant a_0$ and $b \geqslant b_0$. Each ASR has a specific lifetime, e.g., the ASR of GC 6 has a short lifetime of 0.76 s. However, note that we do not need to model the lifetime in the simulation, because the ASR is "dead" when the ASR is outside the area of corresponding GC.

- **The spatial distribution in the ASR**

The spatial density of scatterers in the ASR of r^{th} GC could be expressed as

$$\rho_{S,r}(t) = \frac{L_{S,r}(t)}{S_{ASR,r}(t) \bigcap S_{GC,r}}, \tag{7}$$

where $S_{ASR,r}(t)$ is the area of the ASR, and $S_{GC,r}$ is the area of r^{th} GC. Hence, the distribution of scatterers is

TABLE II: THE GEOMETRICAL PARAMETERS OF ASR

Parameters	ASR1	ASR2	ASR3	ASR4	ASR5	ASR6	ASR7
$C_{S,r,x,0}$ (m)	202.1	613.0	747.6	924.0	984.6	1111.0	1167.5
$C_{S,r,y,0}$ (m)	−24.6	−1.0	−135.0	−192.1	−167.0	−280.4	−310.5
$v_{S,r,0}$	0.33	0.27	0.03	0.15	0.31	0.54	0.79
$\phi_{S,r}$ (degree)	95.0	140.2	161.6	125.3	124.7	152.7	152.0
$R_{S,r}$ (m)	53.3	25.5	6.1	6.2	7.1	7.3	6.8
$\rho_{S,r}$ (/m^2)	0.011	0.021	0.20	0.19	0.14	0.34	0.48
$\mu_{S,r}$ (dB)	−23.4	−17.4	−14.6	−14.1	−14.1	−23.5	−24.0
$\sigma_{S,r}$ (dB)	5.5	3.0	2.7	2.2	2.4	7.2	6.9

$r = \{1, \cdots, 7\}$.

TABLE III: THE GEOMETRICAL PARAMETERS OF GC

Parameters	GC1	GC2	GC3	GC4	GC5	GC6	GC7
$O_{S,r,x}$ (m)	276.0	641.3	752.0	929.7	985.0	1112.4	1181.4
$O_{S,r,y}$ (m)	−35.7	−58.5	−142.8	−186.0	−166.1	−279.3	−334.6
$\theta_{S,r}$ (degree)	112.9	135.6	161.3	156.8	126.6	152.4	154.0
$a_{S,r}$ (m)	59.6	27.0	9.0	8.6	13.0	6.1	6.6
$b_{S,r}$ (m)	204.0	120.0	17.1	33.7	82.4	33.1	41.0

$r = \{1, \cdots, 7\}$.

determined by the interaction of the area of the ASR and the GC. For simplicity, we use the average density to model the distribution of scatterers as $\rho_{S,r} = E[\rho_{S,r}(t)]$, where $E[\cdot]$ denotes statistical expectation. For the sake of tractability [27]-[29], the scatterers are assumed to be distributed uniformly inside the GC in our model, with the estimated density.

For simplicity, a circular region is used to model the ASR, and the radius could be obtained as

$$R_{S,r} = \sqrt{\frac{\widetilde{L}_{S,r}}{\pi \rho_{S,r}}}, \tag{8}$$

where $\widetilde{L}_{S,r}$ is the mean number of active scatterers in the ASR of r^{th} GC. Note that modeling changes of radius is generally difficult, and the fluctuation of radius is small, so that the radius is assumed to be constant.

• The energy distribution in the ASR

Considering that there are few active scatterers in each observation time, the normalized gains of MPCs are combined to analyze their distribution. Based on the measured data, the gain of l^{th} scattering path in the ASR of the r^{th} GC can be expressed as

$$G_{S,r,l}(t) = k_{S,r,l} \cdot G_{S,r}(t), \tag{9}$$

where $k_{S,r,l}$ is a lognormal random variable, more precisely, is a realization of a random variable following a distribution $10 \cdot \log_{10}(k_{S,r,l}) \sim N(\mu'_{S,r}, \sigma^2_{S,r})$, and $\mu'_{S,r}$ and $\sigma_{S,r}$ are the estimated parameters in dB. Fig. 9 depicts the empirical distribution of the normalized gain of MPCs in GC 2, and the estimated probability distribution function (PDF) matches the empirical distribution well. With the condition of $E\left[\sum_{l=1}^{\widetilde{L}_{S,r}} k_{S,r,l}\right] = 1$ and the relationship between lognormal distribution, the adjusted mean can be expressed as

$$\mu_{S,r} = -\frac{10}{\ln 10}\left[\ln(\widetilde{L}_{S,r}) + \frac{\sigma^2_{S,r}}{2(10/\ln 10)^2}\right]. \tag{10}$$

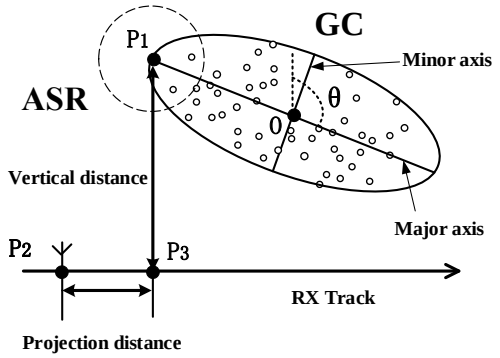

Fig. 10: The geometrical structure of a GC.

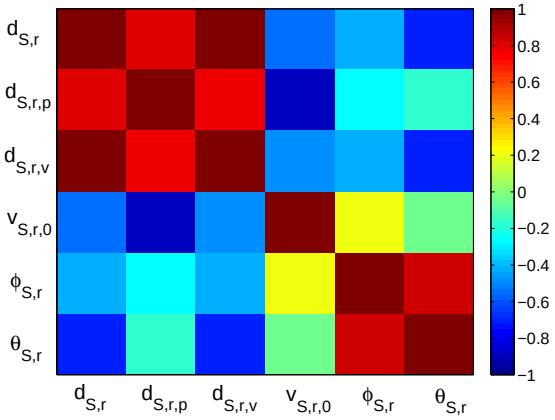

Fig. 11: The correlation coefficients between the parameters.

The extracted parameters of the ASRs are summarized in Table II.

• The shape of the GC

Since the scatterers in a GC are distributed along the buildings or mountains, it is better to model the GC as an ellipsoid in space. As illustrated in Fig. 10, the GC is characterized with central positions $\vec{\boldsymbol{O}}_{S,r}$, minor axis $a_{S,r}$, major axis $b_{S,r}$ and orientation $\theta_{S,r}$, so that the border of the GC can be expressed as

$$\begin{bmatrix} x_{GC,r} \\ y_{GC,r} \end{bmatrix} = \begin{bmatrix} cos(\theta_{S,r}) & sin(\theta_{S,r}) \\ -sin(\theta_{S,r}) & cos(\theta_{S,r}) \end{bmatrix} \begin{bmatrix} a_{S,r} cos(\varphi) \\ b_{S,r} sin(\varphi) \end{bmatrix} + \begin{bmatrix} O_{S,r,x} \\ O_{S,r,y} \end{bmatrix} \tag{11}$$

where $\vec{\boldsymbol{O}}_{S,r} = [O_{S,r,x}, O_{S,r,y}]$ denotes the center of r^{th} GC, and φ is the variable from 0 to 2π. Obviously, the scatterers are distributed inside the region of GC.

The extracted parameters of GC are summarized in Table III. Note that the parameters in Table III are associated with that in Table II, for example, most of the minor axes are similar to, but larger than, the radii of the ASRs, because the rotation of the ellipsoid decreases the minor axis. More details about the geometrical relationships are described in the following.

• The geometrical relationship

As depicted in Fig. 10, there are some important geometrical parameters to express the relationship between the ASR and the GC. $\vec{\boldsymbol{P}}_1$ is regarded as the first center of ASR during lifetime, $\vec{\boldsymbol{P}}_2$ denotes the location of RX at the first observation time, and the projection of $\vec{\boldsymbol{P}}_1$ on the RX track is $\vec{\boldsymbol{P}}_3$. Hence,

the vertical distance and projection distance are defined as $d_{S,r,v} = \|\overrightarrow{\boldsymbol{P_1P_3}}\|$ and $d_{S,r,p} = \|\overrightarrow{\boldsymbol{P_2P_3}}\|$, respectively. The correlation coefficient $\rho_{X,Y}$ between parameters X and Y is calculated as [12]

$$\rho_{X,Y} = \frac{\sum_{r=1}^{R}(X_r - \overline{X})(Y_r - \overline{Y})}{\sqrt{\sum_{r=1}^{R}(X_r - \overline{X})^2 \sum_{r=1}^{R}(Y_r - \overline{Y})^2}}, \tag{12}$$

where $\overline{X}$ and $\overline{Y}$ are the mean values, r denotes the index of the ASR or GC, and R denotes the number of ASR or GC. Fig. 11 depicts the correlation coefficients between the parameters, where red colors and blue colors denote strong positive and negative correlations, respectively. From Fig. 11, we make the following observations:

1) The life distance $d_{S,r}$ is positively correlated to the vertical distance $d_{S,r,v}$ and projection distance $d_{S,r,p}$ with the correlation coefficients of 0.98 and 0.89, respectively. Because the farther the GC is, there is a longer moving distance that the ASR in the GC keeps active and contributes to the channel.
2) The movement direction of ASR $\phi_{S,r}$ is positively correlated to the orientation of GC $\theta_{S,r}$ with the coefficient of 0.82, since the ASR moves along the distributed scatterers in the GC.
3) The movement speed of ASR $v_{S,r,0}$ is correlated to the projection distance $d_{S,r,p}$, because when the scatterers are distributed close to the railway, the ASR will move fast compared to the speed of train, resulting in a negative correlation coefficient of -0.90.

Note that the relationship in geometry will help to simplify our model, i.e., modeling the parameters not deterministically but stochastically with the correlation, but more data is needed to obtain a reliable relationship.

IV. Channel Modeling Results

A. Model overview

In this section, we provide a complete model for a wideband non-stationary channel which includes the following properties:

1) Non-stationary characteristics of the LOS path. The LOS components are influenced by blocking from the poles, so the shadow fading has a periodical character.
2) Non-stationary characteristics of the pole scattering paths. The PS components also have periodic characteristics because of periodically distributed poles along the rail, and the scattered power will change when the receiver gets close to and passes the pole.
3) Non-stationary characteristics of the stochastic geometrical cluster. The ASR of GC will move with the motion of the RX, so that the active scatterers have the birth-and-death process and the lifetime of ASR is finite.

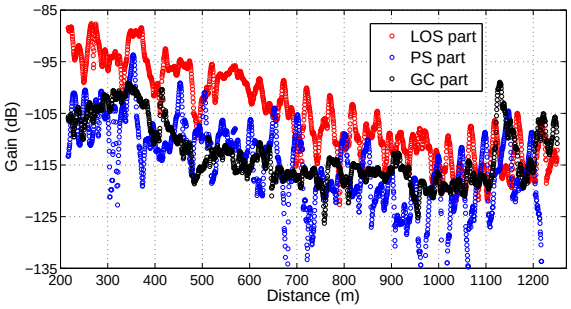

Fig. 12: The gain of three parts along the rail.

Thus, the whole channel impulse response can be divided into three parts as follows,

$$\begin{aligned} h(t,\tau,\theta_T,\theta_R) =& h_{LOS}(t,\tau,\theta_T,\theta_R) + \sum_{k=1}^{K} h_{P,k}(t,\tau,\theta_T,\theta_R) \\ &+ \sum_{r=1}^{R} \xi_{S,r}(t,\tau,\theta_T,\theta_R), \end{aligned} \tag{13}$$

where t, τ, θ_T and θ_R denote the absolute (measurement) time, the delay, the DOD and the DOA, respectively. $h_{LOS}(t,\tau,\theta_T,\theta_R)$ is the LOS component. $h_{P,k}(t,\tau,\theta_T,\theta_R)$ is the PS component, and K is the number of the poles. $\xi_{S,r}(t,\tau,\theta_T,\theta_R)$ is the GC component, and R is the number of the GC.

For each part, we build a double-directional, time-variant and complex impulse response of the channel. The LOS and PS part can be described as

$$\begin{aligned} h_X(t,\tau,\theta_T,\theta_R) =& a_X(t) e^{i\frac{2\pi}{\lambda} c\cdot\tau_X(t) + i\psi_X} \delta(\tau - \tau_X(t)) \\ &\cdot \delta(\theta_T - \theta_{T,X}(t)) \delta(\theta_R - \theta_{R,X}(t)), \end{aligned} \tag{14}$$

where $a_X(t)$, $\tau_X(t)$, $\theta_{T,X}(t)$ and $\theta_{R,X}(t)$ denote the gain, the delay, the DOD and the DOA of the respective MPCs at time t, respectively. Furthermore, λ is the wave length and ψ_X is the additive phase offset, assumed to be uniformly distributed without depending on t. X is $\{LOS\}$ or $\{P,k\}$. The GC part can be modeled as

$$\xi_{S,r}(t,\tau,\theta_T,\theta_R) = a_{S,r}(t) \cdot k_{S,r,l} \sum_{l=1}^{L_{S,r}(t)} \tilde{h}_{S,r,l}(t,\tau,\theta_T,\theta_R), \tag{15}$$

$$\begin{aligned} \tilde{h}_Y(t,\tau,\theta_T,\theta_R) =& e^{i\frac{2\pi}{\lambda} c\cdot\tau_Y(t) + i\psi_Y} \delta(\tau - \tau_Y(t)) \\ &\cdot \delta(\theta_T - \theta_{T,Y}(t)) \delta(\theta_R - \theta_{R,Y}(t)), \end{aligned} \tag{16}$$

where $a_{S,r}(t)$ is the gain of the r^{th} GC, $k_{S,r,l}$ is the normalized factor, $L_{S,r}(t)$ is the number of the active scatterers in the ASR, $\tilde{h}_{S,r,l}(t,\tau,\theta_T,\theta_R)$ represents the normalized components with the similar definition in (14), and Y is $\{S,r,l\}$.

Fig. 12 shows the measured gain of each part with different color dots. The measured data is averaged in a sliding window of 10 samples, to decrease the influence of the small scale fading. The gain of the LOS part as red dots is 10 dB higher than the remaining two parts (i.e., Rice factor $>$ 10 dB), which means that the LOS part dominates the channel impulse response at short distances, though at larger distance the Rice factor is closer to 0 dB and can even become negative. This

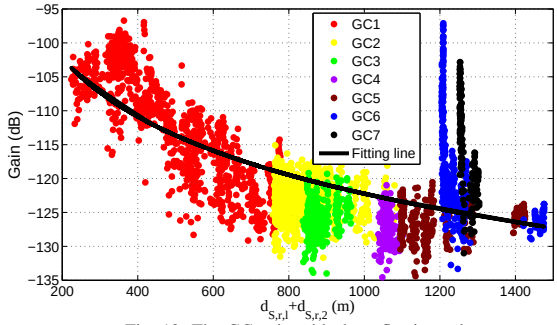

Fig. 13: The GC gain with the reflection rule.

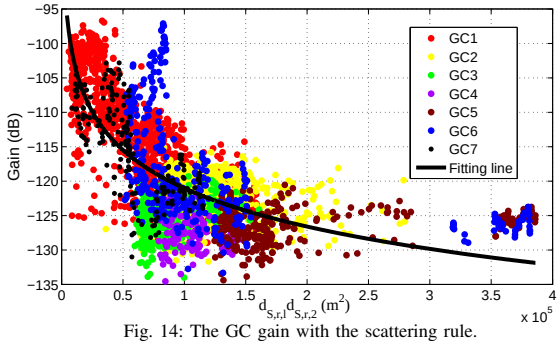

Fig. 14: The GC gain with the scattering rule.

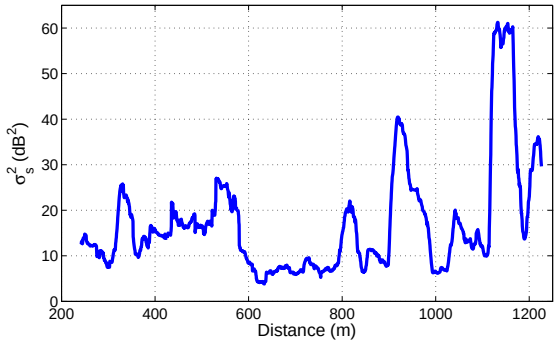

Fig. 15: The mean power of shadow fading along the rail.

is in line with other measurements in the literature [28] [37]. The gains of LOS part and PS part are quasi-periodic, but decreasing with the increasing Tx-Rx distance, and the peaks have a similar period as the spacing of the poles. The gain of the GC part shows non-stationarity since the surroundings are changing as the train moves, for example, the regions around 350 m are the mountains and there are the buildings around 1150 m. In (14) and (15), the gains $a_{LOS}(t)$ of the LOS part, $a_{P,k}(t)$ of the PS part, and $a_{S,r}(t)$ of the GC part are modeled in dB. For space reason, we refer for the details of the modeling of the LOS part and PS part to [10], and we show only the final results here.

B. LOS Gain

The gain of the LOS path can be modeled as a distance-decaying part with the addition of a periodic fading, and the LOS model is expressed as [10]

$$A_L(t) = A_{ref,L} - 10n_L \log_{10}\left(d(t)/d_{ref,L}\right) + S_L(d(t)), \quad (17)$$

$$\begin{aligned} S_L(d(t)) =& a_1(d(t)) + a_2(d(t)) \cdot \sin(\omega d(t) + \Psi_2) \\ &+ a_3(d(t)) \cdot \sin(2\omega d(t) + \Psi_3), \end{aligned} \quad (18)$$

where $d(t)$ is the propagation distance of the LOS path at time t, $A_{ref,L}$ is the power gain at a reference distance $d_{ref,L}$, and n_L is the path loss exponent. $S_L(d(t))$ is the large scale fading, where a_i has a lognormal distribution with variance $\sigma^2_{L,i}$, a_1 relates to the static part of fading, a_2 and a_3 relate to the periodic part of the fading, ω is the fluctuation frequency of the LOS obstruction and Ψ_i is the phase offset. Since the distance d_{p-p} between adjacent poles is 50 m, the value of the periodic parameter corresponds to $\omega = 2\pi/d_{p-p}$, representing the periodic fading characteristics of the poles. The autocorrelation function of each part could be expressed as

$$r_{L,i}(\Delta d) = \begin{cases} \sigma^2_{L,i} e^{-\frac{\ln 2}{d^2_{L,i}}(\Delta d)^2}, i = 1, & (19) \\ \sigma^2_{L,i} e^{-\frac{\ln 2}{d_{L,i}}(\Delta d)}, i = \{2,3\}, & (20) \end{cases}$$

where $d_{L,i}$ is the de-correlation distance, and Δd is the distance between two positions. The extracted parameters of LOS part are summarized in Table IV.

C. PS Gain

The Pole Scattering model consists of two parts, the path loss from BS to the pole (B2P) and the path loss from pole to receiver (P2R). The PS model is expressed as

$$A_{P,k}(t) = G_k + A_{P,0}(d_k(t)), \quad (21)$$

where $A_{P,k}(t)$ is the power gain of the signal from the k^{th} pole. G_k is the decay factor of the k^{th} pole generated by B2P model, which is expressed as

$$G_k(d_{P,k}) = A_{ref,P} - 10n_k \log_{10}\left(d_{P,k}/d_{ref,P}\right) + S_P(d_{P,k}), \quad (22)$$

where $d_{P,k}$ is the distance between the BS and the k^{th} pole, $A_{ref,P}$ is the power gain at a reference distance $d_{ref,P}$, n_k is the path loss exponent, and $S_P(d_{P,k})$ is the large scale fading for the k^{th} pole. An exponential autocorrelation function is used to model the correlated characteristics, $r_P(\Delta d) = \sigma^2_P e^{-\frac{\ln 2}{d_P}(\Delta d)}$, where d_P is the de-correlation distance and σ^2_P is the variance of the lognormal fading. $A_{P,0}(d_k(t))$ is the scattering factor generated by P2R model as

$$A_{P,0} = \begin{cases} -10n_{p,1} \log_{10}\left(d_k(t)/d_b\right), & d_b < d_k(t) \leqslant d_m \\ -n_{p,2} d_k(t) + \beta, & d_l \leqslant d_k(t) \leqslant d_b, \end{cases} \quad (23)$$

where $d_k(t) = x_k - x(t)$, and x_k is the projection of the k^{th} pole in the railway, $x(t)$ is the position of RX at time t. Note that d_m and d_l are the effective ranges as the poles mainly affect the RX in the vicinity of them, d_b is the distance between the peak position and the projection of the pole. $n_{p,1}, n_{p,2}$ are the estimated values of path loss exponents, $\beta = n_{p,2} d_b$. The extracted parameters of PS part are summarized in Table IV.

D. GC Gain

The gain of the GC components can be expressed based on the path loss model (24) to represent specular reflection, or (25) to represent diffuse scattering,

$$\begin{aligned} A_{S,r}(t) =& A_{ref,S} - 10n_S \log_{10}\left[\left(d_{S,r,1}(t) + d_{S,r,2}(t)\right)/d_{ref,S}\right] \\ &+ X_{S,r}(d(t)), \end{aligned} \quad (24)$$

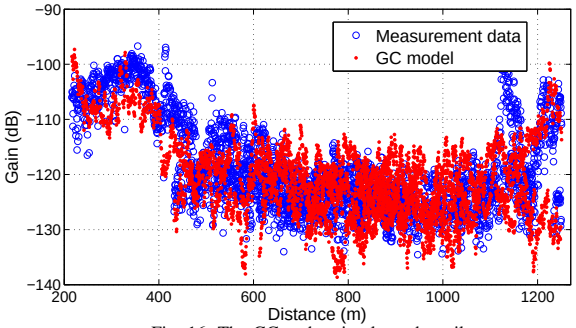

Fig. 16: The GC path gain along the rail.

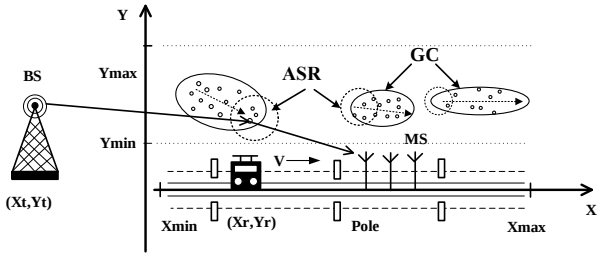

Fig. 17: Geometry for the HSR channel model.

$$A_{S,r}(t) = A_{ref,S} - 10n_S \log_{10}\left[(d_{S,r,1}(t) \times d_{S,r,2}(t))/d_{ref,S}\right] + X_{S,r}(d(t)), \tag{25}$$

where $A_{S,r}(t)$ is the total path gain of the r^{th} GC at time t, $A_{ref,S}$ is the power gain at a reference distance $d_{ref,S}$. $d_{S,r,1}(t)$ is the distance between the BS and the center of the r^{th} ASR, $d_{S,r,2}(t)$ is the distance between the center and the RX. $X_{S,r}$ is the shadow fading (which is assumed to have a lognormal distribution), and $d(t)$ is the propagation distance between TX and RX. Note that in order to simplify the implementation, the distance is only related to the center of the ASR, not the actual position of each active scatterer. Another significant simplification is to fit the path loss of different GCs with the same model, since several of the GCs do not extend over a sufficient distance range to allow a reliable fit of a path loss coefficient. A future model based on larger data sets might model the path loss coefficients as random variables and choose different values for different GCs. The two models (24) and (25) are illustrated with the major detected GCs in Fig. 13 and Fig. 14, respectively. The root-mean-square error (RMSE) between the measured data and the models are 7.8 dB for (24) and 7.2 dB for (25), and the GCs observed in our measurements, i.e., mostly wooded hills, are in line with the physical mechanism of scattering (as opposed to specular reflection), so that we use (25) as the final model. Note that the horizontal axis in Fig. 13 denotes the sum of $d_{S,r,1}$ and $d_{S,r,2}$, while the distance in other plots denotes the propagation distance between BS and MS, i.e., the d_{BS-MS} in Fig. 2.

Once the distance-dependent mean of the total path gain has been removed, the distance autocorrelation function can be expressed as

$$r_S(\Delta d) = E[X_S(d)X_S(d+\Delta d)], \tag{26}$$

where Δd is the distance between two positions, and $X_S(d)$ is the sum of the small-scale averaged contributions at a TX-RX distance d. The most commonly used model is the exponential

TABLE IV: MODEL PARAMETERS OF LOS AND PS

Parameters	LOS	PS
$A_{ref,L}/A_{ref,P}$ (dB)	-86.46	-92.67
n_L/n_k	3.88	3.00
$d_{ref,L}/d_{ref,P}$ (m)	215.7	215.7
$d_{L,i}/d_P$ (m)	$56, 300, 330$	200
d_{p-p}, d_b, d_m, d_l (m)	/	$50, 5, 150, -10$
$n_{p,1}, n_{p,2}$	/	$1.50, -1.80$
Ψ_2, Ψ_3 (degree)	$309, 158$	/
$\sigma^2_{L,i}/\sigma^2_P$ (dB^2)	$0.9, 12.7, 3.0$	20.6

$i = \{1, 2, 3\}$.

TABLE V: MODEL PARAMETERS OF GC

Set	Parameters	GC
Scatterer Distribution	$\vec{O}_{S,r}$	$X_{min} \sim X_{max}, Y_{min} \sim Y_{max}$
	$\theta_{S,r}$ (degree)	$U(110, 160)$
	$a_{S,r}$ (m)	$U(6, 60)$
	$b_{S,r}$ (m)	$U(17, 204)$
	$\rho_{S,r}$ (/m^2)	$U(0.01, 0.5)$
Moving ASR	$v_{S,r,0}$	$U(0.15, 0.8)$
	$\phi_{S,r}$ (degree)	$U(95, 160)$
	$R_{S,r}$ (m)	$U(6, 55)$
	$\mu_{S,r}$ (dB)	$U(-24, -14)$
	$\sigma_{S,r}$ (dB)	$U(2, 7)$
Large-scale fading	n_S	1.85
	$A_{ref,S}$ (dB)	-71.9
	$d_{ref,S}$ (m)	215.7
	μ_S, χ_S (dB)	$2.6, 0.6$
	d_S (m)	8.5

Note that most of the random variables are modeled with uniform distributions based on the measured data.

autocorrelation function [38]

$$r_S(\Delta d) = \sigma_S^2 e^{-\frac{\ln 2}{d_S}(\Delta d)}, \tag{27}$$

where d_S is the de-correlation distance and σ_S^2 is the variance of the lognormal fading distribution. However, unlike the common assumption of stationary variance of the fading, Fig. 15 depicts that σ_S^2 changes with the TX-RX distance, which is caused by the changing environment around the railway. Hence, a stochastic variance should be used for the stochastic lognormal fading, to express the non-WSSUS property in our model. The dynamic process of the shadow fading can be realized recursively by a discrete Gauss-Markov process [39]

$$X_S(d+\Delta d) = \rho(\Delta d)X_S(d) + \sqrt{1-\rho^2(\Delta d)} \cdot \eta, \tag{28}$$

where $\rho(\Delta d) = \exp(-\frac{\ln 2}{d_S}(\Delta d))$ is the correlation level, and η is an uncorrelated variable as $\eta \sim N(0, \sigma_S^2)$. The variance σ_S^2 follows the lognormal distribution based on the measurement data as $\ln(\sigma_S^2) \sim N(\mu_S, \chi_S^2)$. The extracted parameters of GC part are summarized in Table V.

Hence, the gain of the GC model is generated with the path loss model and large scale fading process, and the variance of shadow fading follows the lognormal distribution. To validate the GC model specially, one sample is generated based on the extracted geometrical parameters in Table II and Table III, together with the path loss model parameters in Table V. As

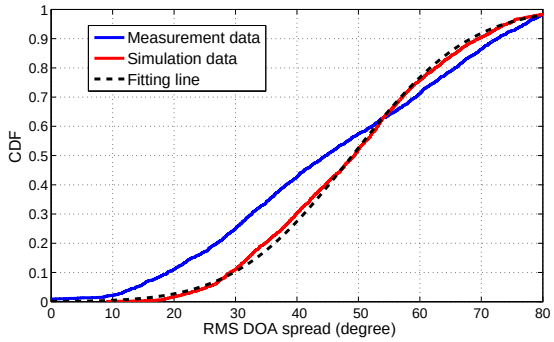

Fig. 18: Example plot of the RMS DOA spread along the rail.

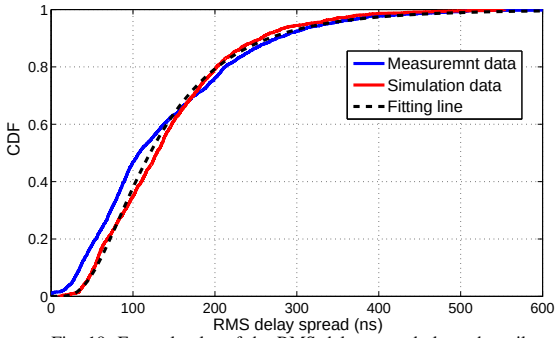

Fig. 19: Example plot of the RMS delay spread along the rail.

depicted in Fig. 16, the new model as red dots match well with the measured result as blue dots.

E. Implementation recipe

An implementation method of the GSCM for HSR can be summarized as follows:

1) **Specify the system**: Specify the velocity of the train, and specify the simulation time, temporal resolution, frequency range and resolution. Note that the carrier frequency is 2.4 GHz, and the velocity of the train is 295 km/h in our measurement.

2) **Model the basic environment**: As depicted in Fig. 17, the railway is regarded as the X axis, and the positive direction is the train moving direction. Specify the physical boundaries of the simulation region $\{\boldsymbol{X}_{min}, \boldsymbol{X}_{max}\}$ and $\{\boldsymbol{Y}_{min}, \boldsymbol{Y}_{max}\}$. Specify the location of BS and the initial location of the MS, and determine their respective location over the simulation period. Specify the locations of the poles based on the spacing d_{p-p}. Nota that the vertical distance between the pole and railway is 1.5 m.

3) **Model the geometry of GC**: Generate coordinates of the center of GC, then determine the minor axis $a_{S,r}$, major axis $b_{S,r}$, orientation $\theta_{S,r}$, and distribution density $\rho_{S,r}$ according to Table V. Generate the coordinates of the scatterers according to uniform distribution inside the elliptical line of the GC.

4) **Model the moving ASR**: There is a moving ASR for each GC, and the bound of GC closest to the RX is regarded as the initialized center of ASR for simplicity. Specify the relative velocity $v_{S,r,0}$, movement direction $\phi_{S,r}$, radius $R_{S,r}$ and energy distribution parameters $\mu_{S,r}$ and $\sigma_{S,r}$ according to Table V, respectively.

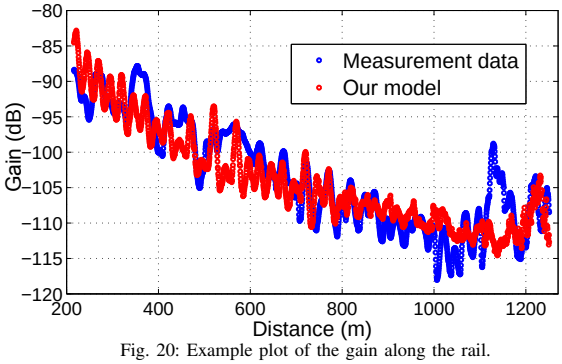

Fig. 20: Example plot of the gain along the rail.

5) **Model the three parts of the channel**: For each time instant, calculate the propagation distance, delay, DOD and DOA of the LOS path, PS path as well as the scattering path from the active scatterer in the ASR of the GC. The path gain is generated based on the path loss model and shadow fading process according to parameters in Table IV and Table V. The complex amplitude of LOS part and PS part are built upon (14), and the GC model is built upon (15)(16). The phase ψ fits a uniform distribution $\psi \sim U(0, 360°)$. Finally, sum up the contribution of the three parts to form the channel impulse response according to (13), which can be further filtered to account for finite bandwidth, and weighted with antenna beam patterns used for the simulations.

V. Model Validation

To validate our proposed model, a simulation of our GSCM for HSR in the hilly scenario is performed, according to the modeling parameters and the implementation steps as above. Since the modeling parameters are direct results obtained from the measurements, secondary parameters root mean square (RMS) DOA spread and RMS delay spread are selected to compare with the measurement data. The RMS DOA spread and RMS delay spread are expressed as

$$\sigma_\theta(t) = \sqrt{\frac{\sum_{i=1}^{N(t)} G_i(t)(\theta_i(t) - \bar{\theta}(t))^2}{\sum_{i=1}^{N(t)} G_i(t)}}, \tag{29}$$

$$\sigma_\tau(t) = \sqrt{\frac{\sum_{i=1}^{N(t)} G_i(t)(\tau_i(t) - \bar{\tau}(t))^2}{\sum_{i=1}^{N(t)} G_i(t)}}, \tag{30}$$

where $G_i(t), \tau_i(t)$ and $\theta_i(t)$ denote the gain, the delay and the DOA of the i^{th} MPC at time t, respectively. $\bar{\tau}(t)$ and $\bar{\theta}(t)$ are the power weighted means of delay and DOA at time t, respectively. $N(t)$ is the total number of LOS path, PS path and the scattering path from GC. Note that the generation of the geometrical environment is mainly based on the extracted parameters in Table II and Table III, since the outcome largely depends on the position of the scatterers. Fig. 18 depicts one sample result of the simulated cumulative distribution function (CDF) of the RMS DOA spread from the proposed model as a red line, the simulation data can be approximated as a normal distribution indicated by the black dashed line. Also, as indicated in Fig. 19, the RMS delay

spread can be approximated to have a lognormal distribution [34]. It is observed that the proposed model as a red line shows a similar manner with respect to the measured data as a blue line. Note that the LOS path is the only path in several measured locations, which contribute a step at 0 for the measured spreads. Finally, Fig. 20 shows the sum of the path gain from the three parts, i.e., LOS part, PS part and GC part, and the simulation also matches the measurement data well.

It is important to note that the outcome can vary significantly in different simulations, due to the dynamic process of the shadow fading and non-stationary property of the channel. The deviation between measurement and the simulation results are largely caused by the simplifications in our model:

- The regular shape to model the ASR and GC is a major simplification since the spatial scatterers are irregularly distributed in the physical environment;
- The single-scattering assumption in our model, as there might be some multi-scattering propagation paths contributions to the channel impulse response;
- The scatterers in the model are assumed to be uniformly distributed with a certain density, and the given density is obtained based on the active scatterers inside the area of ASR, which is associated with the number of estimated paths from the measurement data.

Also note that the above test is not a validation of whether the extracted parameters are representative of other HSR environments. Clearly, large-scale measurements in a variety of locations would be required for such an assessment, which is beyond the scope of the current paper.

VI. Conclusions

This paper provides a generalized GSCM to express the time-variant and non-stationary properties of an HSR channel. The modeling parameters are extracted based on a measurement campaign in the Guangzhou-Shenzhen dedicated high-speed line in a hilly scenario, where the rapid speed, the special construction elements and the rich scattering environment make the HSR channel different from that of other scenarios. High-resolution parameter estimation is used to detect the location of scatterers, and the scatterers associated with the detected components can be divided into two categories: poles and the stochastic GCs. Together with the LOS path, the whole channel impulse response is constructed. The properties of the channel and the basic points for modeling are summarized as follows:

- The periodical fading of the LOS path, the periodical scattering of the poles, and the various scattering of other stochastic scatterers have impact on the total signal;
- The stochastic GCs are the forests, roads, buildings and houses around the rail line. With the movement of the receiver, the active scatterers in the ASR behave in a similar fashion during a long-term period. Each ASR has a specific lifetime since the ASR is "dead" when out of the region of GC, resulting in the time-variant and non-WSSUS properties.

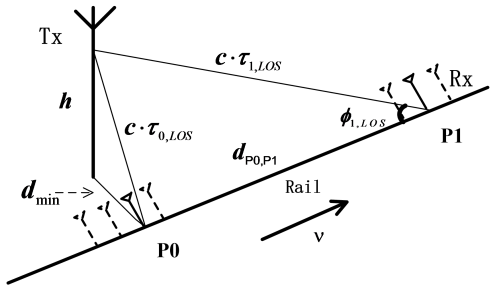

Fig. 21: The scenario for the velocity estimation.

Based on the measurement results, a complete parameterization for modeling the three parts of the HSR channel is proposed, and an implementation recipe is provided, together with the constants or statistical distributions of the modeling parameters. The proposed GSCM is validated by testing the deviation of the RMS DOA spread and RMS delay spread between measured data and simulation result, and reasonable agreement is achieved. Furthermore, the proposed model can be applied in multi-antenna systems since the channel is modeled independent of antenna properties, and the antenna pattern should be taken into consideration for implementation of system design. Future work should obtain more measurement data in different scenarios, to build a complete database for GSCMs in HSRs.

Appendix A

This appendix describes the method for estimating the train velocity, since there is no precision speed data from the train control system directly. Fig. 21 shows the scenario for velocity estimation, h is the relative height between the TX and the RX, and $d_{\min}$ is the horizontal distance between BS and the rail. At the position of P0, the train is just passing by the BS with a Doppler shift of 0. P1 is one of the receiving positions in the far field of the TX. Since the direction of the virtual array is the same as the moving direction, $\phi_{1,LOS}$ is the DOA of the LOS path at P1. Although the SAGE algorithm is applied to extract the delays ($\tau_{0,LOS}$,$\tau_{1,LOS}$) and the Doppler shift ($f_{0,LOS}$,$f_{1,LOS}$) at P0 and P1, the synchronization error should be estimated by comparing the estimation of $\tau_{0,LOS}$ with the calculated result as

$$\tau_{0,LOS} = D/c, \tag{31}$$

where $D = \sqrt{h^2 + d_{min}^2}$, and c is the speed of the light. After the calibration, the values of delays mentioned in this paper are absolute. The estimated velocity v_1 at P1 is calculated as

$$v_1 = \frac{\lambda \cdot f_{1,LOS}}{\cos\phi_{1,LOS}}, \tag{32}$$

where

$$\cos\phi_{1,LOS} = \frac{\sqrt{\tau_{1,LOS}^2 - \tau_{0,LOS}^2}}{\tau_{1,LOS}}, \tag{33}$$

and λ is the wave length of carrier frequency. Since the train velocity is uniform, v_1 is regarded as the estimated train velocity v_{train}.

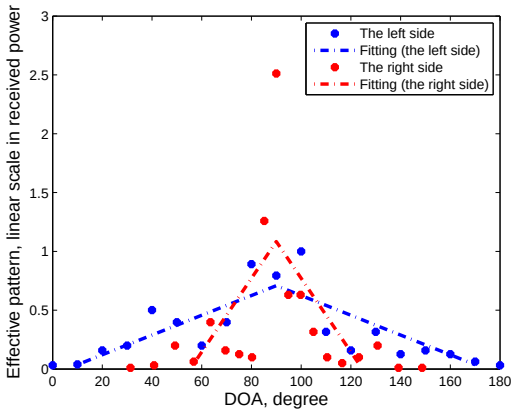

Fig. 22: The "effective" pattern of the receiver.

APPENDIX B

The receiving antenna is fixed on the left window inside the carriage during the measurement campaign, which makes the carriage window become an additive part of the antenna pattern. The total "effective" pattern of the receiving antenna is roughly measured for the incidences from both sides. Fig. 22 depicts the "effective" pattern $f(\theta)$ of the receiver in linear scale, and θ is the DOA. The pattern value is normalized by the maximum received power from the left side incidence. The blue dashed line is the fitting line for the pattern from left side, and the red dashed line is from the right side. The regression lines are expressed as

$$f_{\text{left}}(\theta) = \begin{cases} 0.48\theta - 0.0471 & 0.04\pi \le \theta \le \pi/2 \\ 0.48(\pi - \theta) - 0.0471 & \pi/2 < \theta \le 0.96\pi \\ 0.01 & \text{others}, \end{cases} \quad (34)$$

$$f_{\text{right}}(\theta) = \begin{cases} 1.79\theta - 1.730 & 0.26\pi \le \theta \le \pi/2 \\ 1.79(\pi - \theta) - 1.730 & \pi/2 < \theta \le 0.74\pi \\ 0 & \text{others}. \end{cases} \quad (35)$$

The pattern gain from the left side is larger than that from the right side in the DOA range $\{0 \sim 5\pi/12\}$ and $\{7\pi/12 \sim \pi\}$, which means that the received power mostly comes from the scatterers in the left side of the rail. However, in the DOA range $\{5\pi/12 \sim 7\pi/12\}$, it is difficult to distinguish which side the scattering points come from. Note that when the receiving antenna is fixed on the left window inside or outside the carriage, the average received power from different DOAs are -79.3 dBm and -53.2 dBm, respectively. Hence, the corresponding penetration loss from window is approximately 26 dB.

The DOA estimation is associated with the aperture of virtual array, and the delay estimation is associated with time resolution. Since the SAGE algorithm is a kind of unbiased estimation method, the additive pattern has an impact on the signal-to-noise ratio (SNR) of the MPC, but would not cause an estimation bias. Therefore, the "effective" pattern does not have a strong impact on the estimation of other parameters. For example, assuming that the accurate pattern is unknown, the estimated amplitude and other parameters set are $\{\boldsymbol{A}_1, \boldsymbol{\Omega}_1\}$, and the estimated result is $\{\boldsymbol{A}_2, \boldsymbol{\Omega}_2\}$ when using the accurate pattern. There is a relationship between amplitudes as $\boldsymbol{A}_1 = \Delta A \boldsymbol{A}_2$, and ΔA is the additive pattern. Such pattern causes a bias for amplitude estimation, rather than other parameters set $\boldsymbol{\Omega}_1$ and $\boldsymbol{\Omega}_2$.

REFERENCES

[1] D. Nakagawa and M. Hatoko, "Reevaluation of Japanese high-speed rail construction," *Transport Policy*, vol. 14, no. 2, pp. 150-164, Mar. 2007.

[2] J. Cao, X. C. Liu, Y. Wang, and Q. Li, "Accessibility impacts of Chinas high-speed rail network," *Journal of Transport Geography*, vol. 28, pp. 12-21, Apr. 2013.

[3] M. Aguado, I. Samper, M. Berbineau, and E. Jacob, "4G Communication Technologies for Train to Ground Communication Services: LTE versus WIMAX, a simulation study," *9th World Congress on Railway Research*, pp. 1-10, 2011.

[4] H. Wu, Y. Gu, and Z. Zhong, "Research on the fast algorithm for GSM-R switching for high-speed railway," *J. Railway Eng. Soc.*, no. 1, pp. 92-96, Jan. 2009.

[5] R. Hadani et al., "Orthogonal Time Frequency Space Modulation," *IEEE Wireless Communications and Networking Conference*, pp. 1-6, 2017.

[6] B. Allen et al., "Defining an Adaptable Communications System for all railways," *in proceedings 7th Transport Research Arena TRA 2018*, Vienna, 16-19 April 2018.

[7] F. Y. Luan, Y. Zhang, L. M. Xiao, C. H. Zhou and S. D. Zhou, "Fading Characteristics of Wireless Channel on High-Speed Railway in Hilly Terrain Scenario," *Int. J. Antennas Propag.*, 2013.

[8] Y. Zhang, Z. He, W. Zhang, L. Xiao and S. Zhou, "Measurement-based Delay and Doppler Characterizations for High-speed Railway Hilly Scenario," *Int. J. Antennas Propag.*, 2014.

[9] F. Luan, A. F. Molisch, L. Xiao, F. Tufvesson, and S. Zhou, "Geometrical Cluster-Based Scatterer Detection Method with the Movement of Mobile Terminal," *IEEE Vehicular Technology Conference (VTC Spring)*, pp. 1-6, 2015.

[10] L. Zhou, Z. Yang, F. Luan, A. F. Molisch, F. Tufvesson, and S. Zhou, "Dynamic Channel Model with Overhead Line Poles for High-Speed Railway Communications," *IEEE Antennas Wireless Propag. Lett.*, vol. 17, no. 5, pp. 903-906, 2018.

[11] G. Acosta-Marum and M. A. Ingram, "A BER-based partitioned model for a 2.4GHz vehicle-to-vehicle expressway channel," *Wireless Personal Commun.*, vol. 37, no. 3, pp. 421-443, 2006.

[12] J. Karedal, F. Tufvesson, N. Czink, A. Paier, C. Dumard, T. Zemen, C. F. Mecklenbrauker and A. F. Molisch, "A Geometry-Based Stochastic MIMO Model for Vehicle-to-Vehicle Communications," *IEEE Trans. on Wireless Comm.*, vol. 8, no. 7, pp. 3646-3657, 2009.

[13] L. Liu, C. Tao, J. Qiu, H. Chen, L. Yu, W. Dong and Y. Yuan, "Position-based modeling for wireless channel on high-speed railway under a viaduct at 2.35 GHz," *IEEE Journal on Selected Areas in Communications*, vol. 30, pp.834-845, May. 2012.

[14] R. He, Z. Zhong, B. Ai, G. Wang, J. Ding and A. F. Molisch, "Measurements and analysis of propagation channels in high-speed railway viaducts," *IEEE Trans. on Wireless Comm.*, vol. 12, no.2, pp. 794-805, 2013.

[15] J. Ding, L. Zhang, J. Yang, B. Sun, and J. Huang, "Broadband Wireless Channel in Composite High-Speed Railway Scenario: Measurements, Simulation, and Analysis," *Wireless Communications and Mobile Computing*, pp. 1-15, 2017.

[16] J. Minghua, "A Modified Method for Predicting the Radio Propagation Characteristics in Tunnels," *IEEE International Conference on Wireless Communications, Networking and Mobile Computing*, pp. 1-4, 2011.

[17] A. Hrovat, G. Kandus, and T. Javornik, "A Survey of Radio Propagation Modeling for Tunnels," *IEEE Communications Surveys & Tutorials*, no. 99, pp. 1-12, 2013.

[18] R. He, Z. Zhong, B. Ai, J. Ding, Y. Yang, and A. F. Molisch, "Short-term fading behavior in high-speed railway cutting scenario: measurements, analysis, and statistical models," *IEEE Trans. Antennas Propag.*, vol. 61, no. 4, pp. 2209-2222, 2013.

[19] R. He, Z. Zhong, B. Ai, and J. Ding, "Propagation measurements and analysis for high-speed railway cutting scenario," *Electron. Lett.*, vol. 47, no. 21, pp. 1167-1168, Oct. 2011.

[20] B. Zhang, Z. Zhong, R. He, F. Tufvesson, and B. Ai, "Measurement-Based Multiple-Scattering Model of Small-Scale Fading in High-Speed Railway Cutting Scenarios," *IEEE Antennas Wireless Propag. Lett.*, vol. 16, pp. 1427-1430, 2017.

[21] A. F. Molisch, A. Kuchar, J. Laurila, K. Hugl and R. Schmalenberger, "Geometry-based directional model for mobile radio channels-priciples and implementation," *European Trans. Telecommun.*, vol. 14, pp. 351-359, 2003.

[22] A. F. Molisch, "A generic channel model for MIMO wireless propagation channels in macro-and microcells," *IEEE Trans. Signal Processing*, vol. 52, no. 1, pp. 61-71, Jan. 2004.

[23] X. Cheng, C. X. Wang, D. I. Laurenson, S. Salous and A. V. Vasilakos, "An Adaptive Geometry-Based Stochastic Model for Non-Isotropic MIMO Mobile-to-Mobile Channels," *IEEE Trans. on Wireless Comm.*, Vol. 8, No. 9, pp. 4824-4835, 2009.

[24] T. Zhou, C. Tao, S. Salous, and L. Liu, "Measurements and Analysis of Angular Characteristics and Spatial Correlation for High-Speed Railway Channels," *IEEE Transactions on Intelligent Transportation Systems*, vol. 19, no. 2, pp. 357-367, Feb. 2018.

[25] J. Yang, B. Ai, D. He, L. Wang, Z. Zhong, and A. Hrovat, "A Simplified Multipath Component Modeling Approach for High-Speed Train Channel Based on Ray Tracing," *Wireless Communications and Mobile Computing*, vol. 2017, pp. 1-14, 2017.

[26] J. Guiyuan, W. Muqing, Z. Min, and Z. Ruojun, "A 3-D Channel Model for High-Speed Railway Communications in Mountain Scenario," *The Proceedings of the Second International Conference on Communications, Signal Processing, and Systems*, vol. 246, pp. 1173-1181, 2014.

[27] L. Feng, P. Fan, C. Wang, and A. Ghazal, "A 3D GBSM for high-speed train communication systems under deep cutting scenarios," *International Workshop on High Mobility Wireless Communications*, pp. 86-90, 2015.

[28] B. Chen, Z. Zhong, B. Ai, and D. G. Michelson, "A Geometry-Based Stochastic Channel Model for High-Speed Railway Cutting Scenarios," *IEEE Antennas Wireless Propag. Lett.*, vol. 14, pp. 851-854, 2015.

[29] B. Chen and Z. Zhong, "Geometry-Based Stochastic Modeling for MIMO Channel in High-Speed Mobile Scenario," *Int. J. Antennas Propag.*, vol. 2012, pp. 1-6, 2012.

[30] A. Ghazal, C.-X. Wang, B. Ai, D. Yuan, and H. Haas, "A Nonstationary Wideband MIMO Channel Model for High-Mobility Intelligent Transportation Systems," *IEEE Transactions on Intelligent Transportation Systems*, vol. 16, no. 2, pp. 885-897, Apr. 2015.

[31] A. Ghazal et al., "A Non-Stationary IMT-Advanced MIMO Channel Model for High-Mobility Wireless Communication Systems," *IEEE Trans. on Wireless Comm.*, vol. 16, no. 4, pp. 2057-2068, Apr. 2017.

[32] J. Zhao, S. Wang, X. Liu, Y. Gong, "Geometry-Based Stochastic Modeling for Non-Stationary High-Speed Train MIMO Channels," *IEEE Vehicular Technology Conference (VTC-Fall)*, pp. 1-5, 2016.

[33] L. Liu, J. Poutanen, F. Quitin, K. Haneda, F. Tufvesson, P. D. Doncker, P. Vainikainen and C. Oestges, "The COST 2100 MIMO Channel Model," *IEEE Wireless Communications*, vol. 19, no. 6, pp. 92-99, Dec. 2012.

[34] A. F. Molisch, H. Asplund, R. Heddergott, M. Steinbauer, and T. Zwick, "The COST259 Directional Channel Model-Part I: Overview and Methodology," *IEEE Trans. on Wireless Comm.*, vol. 5, no. 12, pp. 3421-3433, Dec. 2006.

[35] Y. Rui, Y. Zhang, S. Liu and S. Zhou, "3.52-GHz MIMO Radio Channel Sounder," *International Conference on Communications, Circuits and Systems (ICCCAS)*, pp. 79-83, 2008.

[36] B. H. Fleury, M. Tschudin, R. Heddergott, D. Dahlhaus, and K. I. Pedersen, "Channel Parameter Estimation in Mobile Radio Environments using the SAGE Algorithm," *IEEE Journal on Selected Areas in Communications*, vol. 17, no. 3, pp. 434-450, 1999.

[37] R. He, Z. Zhong, B. Ai, and J. Ding, "Distance-Dependent Model of Ricean K-Factors in High-Speed Rail Viaduct Channel," *IEEE Vehicular Technology Conference (VTC Fall)*, pp. 1-5, 2012.

[38] M. Gudmundson, "Correlation model for shadow fading in mobile radio systems," *Electronics Letters*, vol. 27, no. 23, pp. 2145-2146, Nov. 1991.

[39] M. Hu, Z. Zhong, M. Ni, and R. He, "Analysis of Link Lifetime With Auto-Correlated Shadowing in High-Speed Railway Networks," *IEEE Communications Letters*, vol. 19, no. 12, pp. 2106-2109, Dec. 2015.

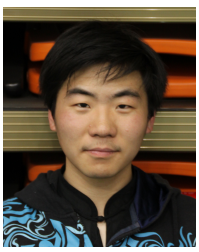

Lai Zhou received the B.S. and Ph.D. degrees from Tsinghua University, Beijing, China, in 2013 and 2018, respectively. Since January 2019, he has been a Postdoctoral Research Assistant in Quantum Communication with the Department of Engineering Science, the University of Oxford, UK. His current research interests include channel modeling, stochastic geometry theory, heterogeneous networking and quantum communication.

Fengyu Luan received the Ph.D. degree from Tsinghua University, Beijing, China, in 2015. He is now working as a senior R&D engineer in the State Grid Ziguang Microelectronics Technology Limited Company. His current research interests include electric power private telecommunication network, wireless communication IC design.

Shidong Zhou (M'98) received B.S. and M.S. degrees from Southeast University, Nanjing, China, in 1991 and 1994, respectively, and the Ph.D. degree from Tsinghua University, Beijing, China, in 1998. He is currently a Professor with the Department of Electronic Engineering, Tsinghua University. He was involved in Program for New Century Excellent Talents in University 2005 (Ministry of Education). He received the Special Award of 2016 National Prize for Progress in Science and Technology. His research interest lies in wireless transmission techniques, including distributed wireless communication system, channel sounding and modeling, coordination of communication, control and computingand application in future mobile communications.

Andreas F. Molisch (S'89-M'95-SM'00-F'05) received the Dipl. Ing., Ph.D., and habilitation degrees from the Technical University of Vienna, Vienna, Austria, in 1990, 1994, and 1999, respectively. He subsequently was with AT&T (Bell) Laboratories Research (USA); Lund University, Lund, Sweden, and Mitsubishi Electric Research Labs (USA). He is now a Professor and the Solomon Golomb - Andrew and Erna Viterbi Chair at the University of Southern California, Los Angeles, CA, USA.

His current research interests are the measurement and modeling of mobile radio channels, multi-antenna systems, wireless video distribution, ultra-wideband communications and localization, and novel modulation formats. He has authored, coauthored, or edited four books (among them the textbook Wireless Communications, Wiley-IEEE Press), 19 book chapters, more than 230 journal papers, more than 320 conference papers, as well as more than 80 patents and 70 standards contributions.

Dr. Molisch has been an Editor of a number of journals and special issues, General Chair, Technical Program Committee Chair, or Symposium Chair of multiple international conferences, as well as Chairman of various international standardization groups. He is a Fellow of the National Academy of Inventors, Fellow of the AAAS, Fellow of the IET, an IEEE Distinguished Lecturer, and a Member of the Austrian Academy of Sciences. He has received numerous awards, among them the Donald Fink Prize of the IEEE, the IET Achievement Medal, the Armstrong Achievement Award of the IEEE Communications Society, and the Eric Sumner Award of the IEEE.

Fredrik Tufvesson (S'97CM'04CSM'07CF'17) received his Ph.D. in 2000 from Lund University in Sweden. After two years at a startup company, he joined the department of Electrical and Information Technology at Lund University, where he is now professor of radio systems. His main research interest is the interplay between the radio channel and the rest of the communication system with various applications in 5G systems such as massive MIMO, mm wave communication, vehicular communication and radio based positioning.

Fredrik has authored around 80 journal papers and 140 conference papers, he is fellow of the IEEE and recently he got the Neal Shepherd Memorial Award for the best propagation paper in IEEE Transactions on Vehicular Technology and the IEEE Communications Society best tutorial paper award.